ACS APPLIED MATERIALS & INTERFACES

Research Article

www.acsami.org

DNA-Hybrid-Gated Photothermal Mesoporous Silica Nanoparticles for NIR-Responsive and Aptamer-Targeted Drug Delivery

Yuanxin Zhang,[†,§] Zhiyao Hou,[†] Yakun Ge,[§] Kerong Deng,[†,‡] Bei Liu,[†,‡] Xuejiao Li,[†,‡] Quanshun Li,[#] Ziyong Cheng,[†] Ping'an Ma,[†] Chunxia Li,[*,†] and Jun Lin[*,†]

[†]State Key Laboratory of Rare Earth Resource Utilization, Changchun Institute of Applied Chemistry, Chinese Academy of Sciences, Changchun 130022, P. R. China

[§]College of Biology and Food Engineering, Jilin Institute of Chemical Technology, Jilin 132022, P. R. China

[‡]University of Chinese Academy of Sciences, Beijing 100049, P. R. China

[#]School of Life Science, Jilin University, Changchun 130012, P. R. China

Supporting Information

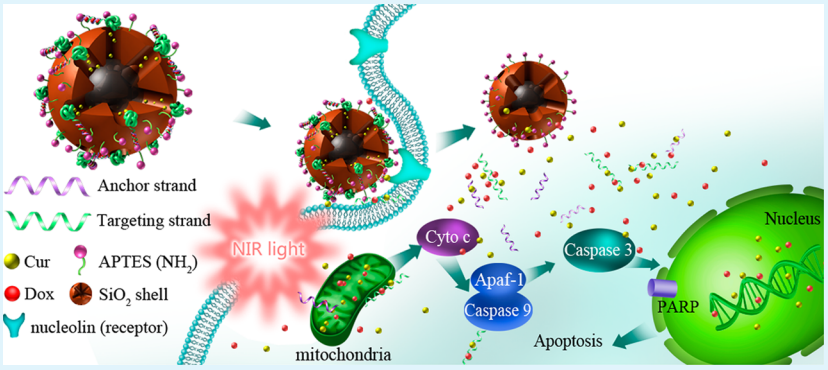

ABSTRACT: Near-infrared light is an attractive stimulus due to its noninvasive and deep tissue penetration. Particularly, NIR light is utilized for cancer thermotherapy and on-demand release of drugs by the disruption of the delivery carriers. Here we have prepared a novel NIR-responsive DNA-hybrid-gated nanocarrier based on mesoporous silica-coated $Cu_{1.8}S$ nanoparticles. $Cu_{1.8}S$ nanoparticles, possessing high photothermal conversion efficiency under a 980 nm laser, were chosen as photothermal agents. The mesoporous silica structure could be used for drug storage/delivery and modified with aptamer-modified GC-rich DNA-helix as gatekeepers, drug vectors, and targeting ligand. Simultaneously, the as-produced photothermal effect caused denaturation of DNA double strands, which triggered the drug release of the DNA-helix-loaded hydrophilic drug doxorubicin and mesopore-loaded hydrophobic drug curcumin, resulting in a synergistic therapeutic effect. The $Cu_{1.8}S@mSiO_2$ nanocomposites endocytosed by cancer cells through the aptamer-mediated mode are able to generate rational release of doxorubicin/curcumin under NIR irradiation, strongly enhancing the synergistic growth-inhibitory effect of curcumin against doxorubicin in MCF-7 cells, which is associated with a strong mitochondrial-mediated cell apoptosis progression. The underlying mechanism of apoptosis showed a strong synergistic inhibitory effect both on the expression of Bcl-2, Bcl-xL, Mcl-1, and upregulated caspase 3/9 activity and on the expression level of Bak and Bax. Therefore, $Cu_{1.8}S@mSiO_2$ with efficient synergistic therapeutic efficiency is a potential multifunctional cancer therapy nanoplatform.

KEYWORDS: *NIR light, copper sulfide, photothermal conversion, synergistic effect, mesoporous silica, aptamer*

INTRODUCTION

The advancement of nanomedicine is currently focused on amplifying in vivo stability and pharmacokinetics of formulations in an effort to enhance drug delivery.[1] However, traditional cancer chemotherapy accompanied by side effects to the patient and multidrug resistance (MDR) play a significant role in hampering therapeutic efficacy and could result in undesirably low penetration.[2,3] Specifically, most chemotherapeutic drugs have to be used at maximum tolerated dose (MTD) to gain a clinical meaningful therapeutic efficacy.[3] Therefore, an ideal solution to improve the therapeutic index of anticancer drugs would both reduce the minimum effect dose (MED) and raise MTD. The application of combination therapy can be achieved through nanoparticle codelivery of an antitumor drug along with a sensitizer.[4−7] The synergistic action between two drugs can improve treatment response and minimize the development of resistance or adverse events.[8] Therefore, nanoparticle formulations, which are able to carry

Received: June 23, 2015
Accepted: September 1, 2015
Published: September 1, 2015

DOI: 10.1021/acsami.5b05522
ACS Appl. Mater. Interfaces 2015, 7, 20696−20706

Scheme 1. Synthetic Process, Anticancer Drug Loading, and Possible Receptor-Mediated Endocytosis Pathway of the Targeting $Cu_{1.8}S$@$mSiO_2$ Core−Shell NCs

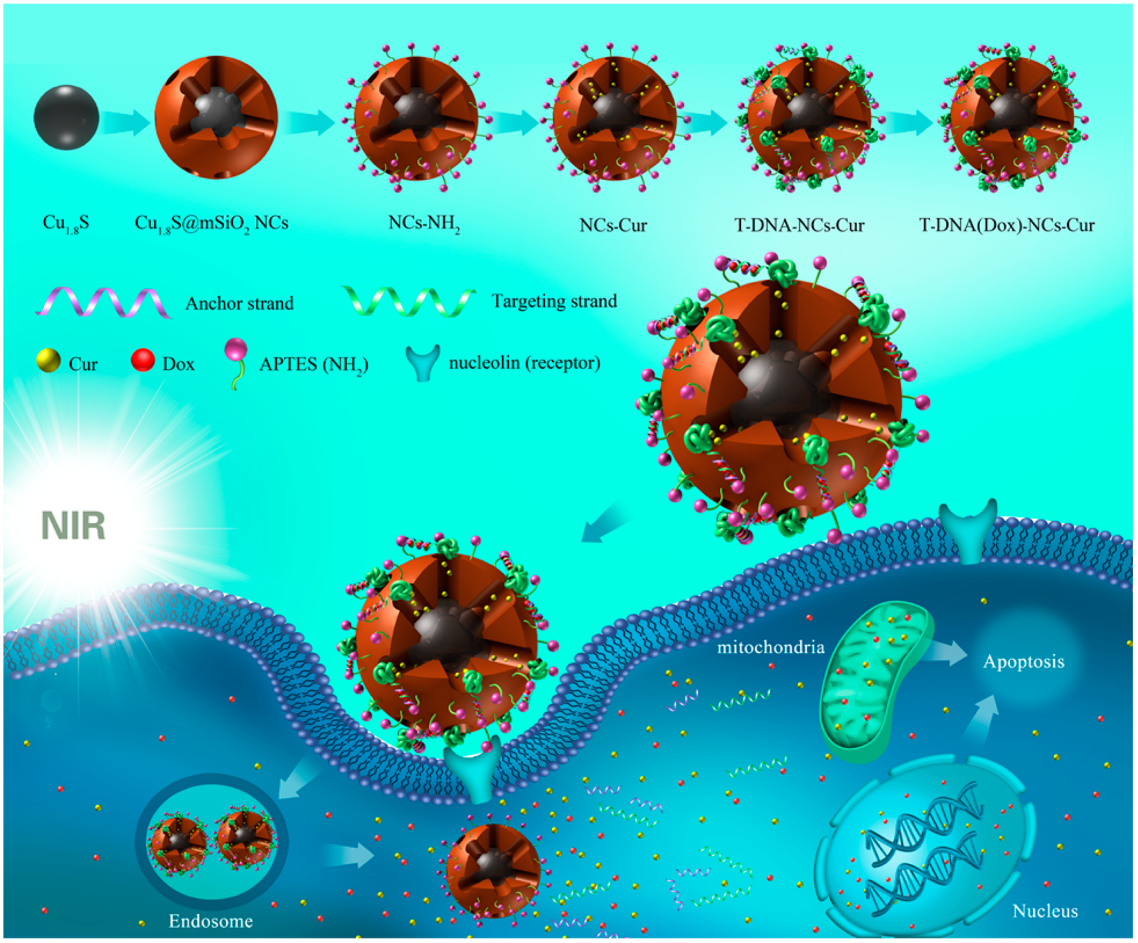

and deliver various drugs with different physicochemical properties while processing stimulus-responsive and targeting-delivery capability, are highly desired.

Curcumin (Cur), a dietary polyphenol constituent, inhibits tumor cell growth through decreasing the expression level of nuclear factor-kappaB (NFκB), ATP-binding cassette (ABC) drug transporters, and antioncogenes, e.g., Bcl-2 and Bcl-xL.[9−14] Recent studies have shown that Cur also synergizes the therapeutic potential of doxorubicin (Dox) coencapsulated in poly(butyl cyanoacrylate) nanoparticles (PBCA NPs), reversing MDR through decreasing the expression level of P-glycoproteins in MCF-7/ADR cells.[15] While Cur cannot be effectively used in clinical application due to the low water solubility and poor bioavailability, its hydrophobicity can be utilized to facilitate the encapsulation of Cur into mesoporous silica nanoparticles (MSNs).[16,17] Consequently, combination therapy of both Cur and Dox can employ synergy between the two drugs for enhancing antitumor efficacy. However, current efforts on encapsulating Cur and Dox into mesopores of MSNs are severely limited owing to some main problems associated with burst drug release and different polarities of drug molecules.

Previously, various drug delivery carriers based on MSNs have been fabricated on the basis of their mesoporous structure, large surface area and pore volume, high loading capacity, functionalization at their outer and/or inner surface, and tunability of their pore geometry.[18] Furthermore, MSNs are effective carriers for achieving "zero" premature release of drugs and obtaining high local concentrations of the drug at the target site by employing nanoparticles, supramolecular assemblies, polymer multilayers, DNA, or proteins as gatekeepers.[19−23] Especially, DNA double strands, which contain sequential GC base pairs, provide loading sites for Dox.[24] By changing the number of GC base pairs, Dox-loading can be exactly adjusted.[25] Apart from serving as a Dox-loading scaffold, one thiolated DNA strand (denoted as anchor strand) is capable of anchoring to the surface of nanocomposites, and the complementary strand (denoted as targeting strand) is preconjugated with an aptamer for targeting delivery and zero premature release. Therefore, an aptamer-modified guanine-rich DNA segment can be utilized as a drug carrier for a combination of multidrugs[26] or drug/gene to give rise to a synergistic effect.[27]

Besides the above advantages, researchers are exploring the possibility of integrating NIR light, which is highly attractive due to high detection sensitivity, increased image contrast, decreased damage to live cells, and deep tissue penetration,[28−31] in controlled drug-delivery systems. The combination of synergistic chemotherapy, on-demand drug release, and targeting delivery would obtain optimal therapeutic effect in cancer therapy. For example, Yuan et al.[32] have fabricated sgc8-guided, G-quadruplex DNA-conjugated, photosensitizer-loaded upconversion nanoparticles, which integrates the beneficial features of the DNA aptamer and NIR light to develop an

DOI: 10.1021/acsami.5b05522
ACS Appl. Mater. Interfaces 2015, 7, 20696−20706

intelligent cancer-specific imaging and NIR-triggered photodynamic therapy (PDT) nanoplatform. Another method for fabricating targeted NIR-stimulus nanoparticles requires copper-based photothermal materials including copper sulfide[33] and copper selenide[34] as NIR light-to-heat transducers for denaturing the DNA double stands under NIR light irradiation and triggering the release of loaded drugs at the target site for combination therapy. Most notably, DNA hybridization on silica-coated nanocomposite surfaces enhances the solubility of nanoparticles due to the amphiphilic nature.[35] Besides, the aptamer can be utilized as a "gatekeeper" to protect the premature release of loaded drug.[36]

Herein we report the design and construction of NIR-responsive controlled release systems for two kinds of anticancer drugs by using mesoporous silica-coated $Cu_{1.8}S$ as nanovehicles. Through covalent conjugation on the surface of $Cu_{1.8}S@mSiO_2$ (denoted as NC), GC-rich DNA-helix and AS1411 could make it possible to load an anticancer drug and target the tumor cell. The synthetic process for T-DNA(Dox)−NC−Cur nanocomposites is summarized in Scheme 1. T-DNA(Dox)−NC−Cur can recognize the tumor cells and penetrate the cell membrane through the receptor-mediated endocytosis pathway. Upon being irradiated with 980 nm laser light, the hybrid nanoplatform T-DNA(Dox)−NC−Cur can release Cur and Dox simultaneously for multiple anticancer therapy, such as combination therapy and targeting delivery. The biocompatibility, drug loading and release, synergistic effects, and apoptotic molecular mechanism for the MCF-7 cells in vitro were investigated in detail.

EXPERIMENTAL SECTION

Materials. Oleylamine (OM, 70%), oleic acid (OA, technical grade, 90%), Cur, 3-(4,5-dimethylthiazol-2-yl)-2,5-diphenyltetrazolium bromide (MTT), and 1-octadecene (ODE, 90%) were purchased from Sigma-Aldrich. Sulfur (99.98%), copper(I) chloride (CuCl, 97%), cetyltrimethylammonium bromide (CTAB, ≥99%), tetraethylorthosilicate (TEOS), sodium hydroxide (NaOH, reagent grade, ≥98%), and ammonium nitrate (NH_4NO_3, ≥99.0%) were obtained from Beijing Fine Chemical Reagent Company (China). Doxorubicin hydrochloride was purchased from Nanjing Duodian Chemical Limited Company (China). Dulbecco's Modified Eagle Medium (DMEM) and FBS were purchased from GIBCO-BRL (Grand Island, NY). Annexin-V−FITC Apoptosis Detection Kit and Caspase Activity Assay Kit were purchased from Bestbio Co. (Shanghai, China). PVDF membrane was purchased from Millipore Co. (Billerica, MA). Antibodies against Pro-caspase-3, Pro-caspase-8, Pro-caspase-9, PARP, Bcl-2, Bcl-xL, Mcl-1, Bax, Bak, apaf-1, cytochrome c, β-actin, and HRP-labeled goat antimouse IgG were obtained from Santa Cruz Biotechnology (Santa Cruz, CA). Unless specified, all the analytical grade chemical reagents were used as received without additional purification.

General Procedure for Preparation of $Cu_{1.8}S@mSiO_2$ Nanoparticles. First, $Cu_{1.8}S$ nanoparticles were fabricated according to a previously published protocol with some modifications.[37] Briefly, 0.5 g of CuCl was mixed with 4 mL of OM and 5 mL of OA, heated to 130 °C, and cooled to room temperature under a nitrogen atmosphere, resulting in the formation of copper precursor. Then 0.16 g of sulfur powder and 40 mL of ODE were added to a three-necked bottle that was connected to a standard Schlenk line. Afterward, when the liquid was heated to 200 °C, copper precursor was injected rapidly into the bottle. The as-obtained black colloidal solution was cooled to 60 °C after 30 min and precipitated with ethanol followed by centrifugation. The resultant $Cu_{1.8}S$ nanoparticles were dissolved in chloroform for further experiments.

Next, surfactant-assisted sol−gel methodology was used to synthesize $Cu_{1.8}S@mSiO_2$ nanocomposites in which the mesoporous silica shell was coated directly onto a single $Cu_{1.8}S$ nanoparticle. A chloroform solution containing $Cu_{1.8}S$ nanoparticles (about 10 mg) was dispersed into a solution of CTAB (0.1 g) in H_2O (30 mL) and sonicated to evaporate the organic solvent, affording CTAB-stabilized $Cu_{1.8}S$ water solution. Then 3 mL of ethanol and 150 μL of NaOH (2 M) were introduced into the above solution. The sample was magnetically stirred and heated to 70 °C before dropwise addition of 150 μL of TEOS. After 2 h of reaction, the as-obtained materials were centrifuged and washed with ethanol. Finally, the surfactant CTAB was removed in NH_4NO_3/ethanol via an ion exchange method so as to obtain $Cu_{1.8}S@mSiO_2$ nanocomposites.[38]

In Vivo Photothermal Imaging of $Cu_{1.8}S@mSiO_2$ Nanoparticles. A 100 μL amount of $Cu_{1.8}S@mSiO_2$ (400 μg/mL) or saline was injected into the subcutaneous tissues of mice bearing H22 tumors, respectively. At different times, the thermal imaging was recorded by a R300SR-HD infrared camera (NEC) with 980 nm laser irradiation at a power density of 1 W cm^{-2}.

Measurement of Photothermal Performance. For determining the temperature change owing to the photothermal conversion of as-obtained $Cu_{1.8}S@mSiO_2$ core/shell nanocomposites, 980 nm NIR laser light was delivered through a quartz cuvette containing an aqueous dispersion (0.3 mL) of different $Cu_{1.8}S@mSiO_2$ core/shell nanocomposite concentrations (i.e., 0, 0.0625, 0.125, 0.25, 0.5 mg mL^{-1}). The light source was an external adjustable 980 nm semiconductor laser device (0−0.3 W) with a 5 mm diameter laser module (Xi'an Tours Radium Hirsh Laser Technology Co., Ltd. China). The output power was independently calibrated using a hand-held optical power meter and was found to be ≈1 W cm^{-2}. A thermal couple with an accuracy of ±0.1 °C was inserted into the aqueous dispersion perpendicular to the path of the laser. The temperature change was measured one time per 30 s.

Preparation of APTES-Conjugated Mesoporous $Cu_{1.8}S@mSiO_2$ Nanospheres. To conjugate the amino functional groups on the mesoporous $Cu_{1.8}S@mSiO_2$ nanospheres, 20 mg of silica-coated copper sulfide sample obtained above was suspended in anhydrous ethanol. After that, a freshly prepared solution of APTES (4.4% w/v) in the desired solvent was added into the sample suspension and the final volume of the suspension was adjusted to 15 mL. Then 15 mL of suspension was refluxed at 80 °C for 12 h under magnetic stirring. After the reaction was finished, the resultant suspension was centrifuged at 12 000 rpm for 15 min and the precipitate was collected. The operation of dispersion and centrifugation was repeated for three cycles. Finally, the resulting precipitate was redispersed into 20 mL of anhydrous ethanol by sonication treatment. Successful amino modification on the surface of $Cu_{1.8}S@mSiO_2$ was confirmed by FT-IR and XPS.

Preparation of T-DNA(Dox)−NC−Cur, Drug Storage, and NIR-Responsive Drug Release in Vitro. The drug Cur was dissolved in EtOH. Then 10 mg of mesoporous APTES−$Cu_{1.8}S@mSiO_2$ nanocompsite was dispersed in 5 mL of (3 mg mL^{-1}) Cur solution and stirred at room temperature under dark conditions for several days. The resultant products were washed quickly three times with EtOH to remove the physically absorbed Cur residue on the surface and collected by centrifugation.

The thiol-anchor strand was coupled to the APTES−$Cu_{1.8}S@mSiO_2$ NCs through Sulfo-SMCC. Excess Sulfo-SMCC (4 mg) was added to a solution mixture of buffer 1 and DMF (7:3 v/v), and then APTES−$Cu_{1.8}S@mSiO_2$ NCs were suspended in this solution for several hours. The resultant samples were collected through centrifugation and extensively washed with DMF and buffer 1 three times. The functionalization of the the thiol-anchor strand was performed by mixing excess anchor strand (15 nM) with the maleimide-modified NCs in conjugation buffer 2 and shaking at room temperature overnight. The particle was recovered by centrifugation and washed with the conjugation buffer. To calculate the conjugation efficiency, all the washing solutions were collected and measured at 260 nm wavelength absorbance using a UV−vis spectrophotometer. After that, targeting strands were incubated with ONT−NC to yield T-DNA−NCs. Two milliliters of T-DNA−NC−Cur sample (5 mg mL^{-1}) was mixed with 2 mL of Dox aqueous solution (1 mg mL^{-1}) and stirred for 24 h under dark conditions. The

DOI: 10.1021/acsami.5b05522
ACS Appl. Mater. Interfaces 2015, 7, 20696−20706

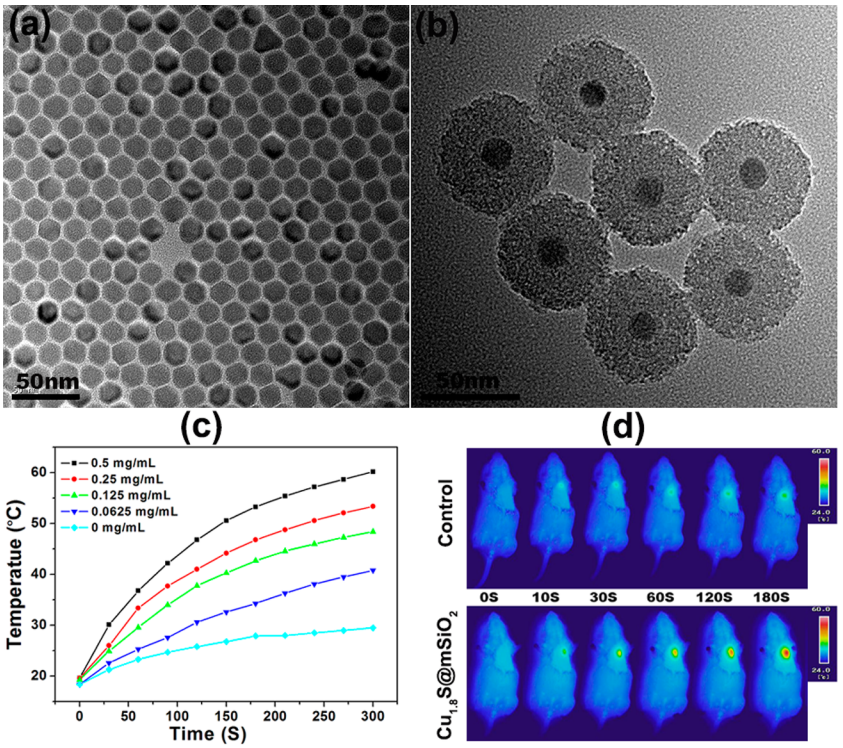

Figure 1. TEM image of $Cu_{1.8}S$ nanoparticles (a) and $Cu_{1.8}S$@$mSiO_2$ nanospheres (b). The temperature variation of aqueous solution containing $Cu_{1.8}S$@$mSiO_2$ nanospheres as a function of irradiation time at various concentrations (0, 0.0625, 0.125, 0.25, and 0.5 mg mL^{-1}) upon irradiation with a NIR laser (980 nm, 1 W cm^{-2}) (c). In vivo infrared thermal imaging of the tumor-bearing Balb/c mice treated with and without the $Cu_{1.8}S$@$mSiO_2$ nanospheres after a 980 nm laser irradiation for 180 s (d).

Dox-loaded sample was collected by centrifugation and denoted as T-DNA(Dox)−NC−Cur. Then T-DNA(Dox)−NC−Cur samples were immersed in 2 mL of pH = 7.4 phosphoric acidic buffer solution (PBS) and irradiated with a 980 nm semiconductor laser device for 5 min at 37 °C with gentle shaking. At predetermined time intervals, samples were subjected to centrifugation, followed by replacing the supernatant with 2 mL of fresh PBS. The amount of released Cur and Dox was analyzed with a UV−vis spectrophotometer at a wavelength of 340 and 480 nm, respectively. To calculate the drug-loading rate, the supernatant and washing liquid were collected and the residual drug content (RD) was obtained by UV−vis measurement at different wavelengths. The loading rate of drugs can be calculated as follows: [(OD − RD)/OD] × 100%, in which OD is the original drug content.

Cell Viability Assays. Cells were seeded into 96-well plates at 5000 cells/well. After culture for 24 h, the cells were treated either with DMSO alone, different doses of Cur (1.5625−400 μM) dissolved in DMSO, different doses of Dox (0.000001−100 μM) dissolved in DMSO, Cur alone, Dox (i.e., 0.001, 0.01, 0.1 μM)−Cur (i.e., 3.125, 6.25, 12.5 μM) combination, NIR irradiation, NCs, T-DNA(Dox)−NC−Cur, or T-DNA(Dox)−NC−Cur plus NIR irradiation for 24 h, followed by adding 5 mg mL^{-1} MTT solution (20 μL/well). After 4 h of incubation, the media containing MTT was removed and 150 μL of DMSO was added into each well to dissolve the formazan crystals. The absorbance was measured at 490 or 570 nm absorbance wavelength with a microplate reader.

Intracellular ROS Detection. A cell-permeable dye of fluorogenic substrate 2,7-dichlorofluorescein diacetate (DCFH-DA), which could be oxidized to the highly fluorescent dichlorofluorescein (DCF) by ROS, was chosen to detect the intracellular generation of ROS. After a 6 h incubation of MCF-7 and HEK-293 cells in the dark with T-DNA(Dox)−NC−Cur, noninternalization NCs were rinsed with PBS, and the fresh culture media containing DCFH-DA (20 μM) were added for another 1 h incubation in the dark. The MCF-7 and HEK-293 cells were then irradiated with a 980 nm NIR laser at a power density of 1 W cm^{-2} for 5 min. Then the irradiated cells were collected by trypsinization, redispersed in PBS after washing three times, and filtered through 35 mm nylon mesh to form a single cell suspension. The intracellular ROS level was analyzed using the FacsCalibur flow cytometer, where the gate was arbitrarily set for the detection of green fluorescent DCF. The excitation wavelength and emission wavelength were 485 and 525 nm, respectively.

Mitochondrial Membrane Potential ($\Delta\Psi_m$) Detection Using JC-1. As the hallmark for cellular apoptosis, the mitochondrial membrane potential (MMP, $\Delta\Psi_m$) was measured using JC-1 (fluorescent cationic dye, 5,5′,6,6′-tetrachloro-1,1′,3,3′-tetraethylbenzimidazolyl-carbocyanine iodide) by detecting a switch from red to green fluorescence. After NIR-triggered treatment and further 3 h incubation, MCF-7 cells (1×10^6) grown on a 35 mm dish were washed twice with PBS and incubated with JC-1 dye in serum-free medium for 20 min at 37 °C. Subsequently, treated cells were rinsed with cold JC-1 buffer solution two times and incubated in fresh medium, and the percentage of low $\Delta\Psi_m$ cells was evaluated by flow cytometry. JC-1-stained MCF-7 cells were dispersed in PBS and analyzed using a FacsCalibur cytometer to assess the percentage of low $\Delta\Psi_m$ cells. The FL-1 channel (*X*-axis) represents the green fluorescence intensity of JC-1 monomers), and the FL-2 channel was used to detect the red fluorescence of JC-1 aggregates. The Q_2 region consists of the low $\Delta\Psi_m$ cell population.

Caspase Activity Assay. Caspase-3, caspase-8, and caspase-9 activation was measured by caspase activity kits according to the manufacturer's protocols. Briefly, after 2 h incubation with T-DNA(Dox)−NC−Cur (250 μg mL^{-1}) at 37 °C in the dark, the cells were irradiated with a 980 nm laser device for 5 min three times (5 min break after 5 min irradiation) and then were incubated for further 24 h at 37 °C in the dark. Subsequently, the cells were scraped with a rubber policeman and collected by centrifugation at 10 000*g* at 4 °C in PBS (0.01 M, pH 7.4). The cell pellet was mixed with 100 μL of lysis buffer. The resulting sample was centrifuged at 10 000*g*, 4 °C, 10 min, and the supernatant was incubated with the supplied reaction buffer, which contained dithiothreitol and substrates, at 37 °C. The change in caspase activity was then determined at 405 nm wavelength using a microplate reader.

DOI: 10.1021/acsami.5b05522
ACS Appl. Mater. Interfaces 2015, 7, 20696−20706

Apoptotic Assay. MCF-7 cells were incubated with T-DNA(Dox)−NC−Cur for 3 h at 37 °C in the dark and then irradiated with a 980 nm laser device for 5 min three times (5 min break after 5 min irradiation). After NIR-triggered treatment of T-DNA(Dox)−NC−Cur, MCF-7 cells were incubated for further 24 h at 37 °C in the dark. Then cells were harvested and washed twice with cold PBS (0.01 M, pH = 7.4). For annexin-V−FITC apoptosis detection, the cells (1×10^6) were rinsed with PBS (0.01 M, pH = 7.4) and then were incubated with binding buffer, containing annexin-V−FITC and PI for 15 min at room temperature in the dark. Next, the cells were analyzed with flow cytometry (BD FACSCalibur). All experiments were performed in triplicate.

Cytosol/Mitochondria Fractionation. After NIR-triggered combinatory therapy, MCF-7 cells were harvested and then fractionated using Cytosol/Mitochondria Fractionation Kit according to the supplier's recommendations. Briefly, the cells were redispersed in a lysis buffer (20 mmol L^{-1} 4-(2-hydroxyethyl)-1-piperazineethanesulfonic acid (HEPES, pH = 7.5), 1.5 mmol L^{-1} $MgCl_2$, 10 mmol L^{-1} KCl, 1 mmol L^{-1} ethylenediaminetetraacetic acid, 1 mmol L^{-1} ethylene glycoltetraacetic acid, 1 mmol·L^{-1} dithiothreitol, 0.1 mmol L^{-1} phenylmethylsulfonyl fluoride, and 250 mmol L^{-1} sucrose) and stirred with a microhomogenizer. The homogenates were collected through 500*g* centrifugation for 10 min at 4 °C, and the resulting supernatants were further centrifuged at 10 000*g* for 15 min at 4 °C. The remaining supernatant was the cytosol fraction, and the precipitation was mitochondrial protein.

Total Protein Extraction. At the end of NIR-triggered combinatory treatment, both adherent and floating MCF-7 cells were harvested, washed twice with cold PBS, and then disrupted in lysis buffer (50 mmol L^{-1} Tris, pH = 8.0, 150 mmol L^{-1} NaCl, 0.1% SDS, 1% NP40, 0.5% sodium deoxycholate, 1% Cocktail, and 1 mmol L^{-1} PMSF) on ice for 30 min. After centrifugation of the cell debris at 10 000*g* for 10 min, protein content was determined via Bradford assay.

Western Blotting Analysis. Protein samples (40 μg) were separated by 12% sodium dodecyl sulfate−polyacrylamide gel electrophoresis (SDS-PAGE) and transferred onto a PVDF membrane for 2 h at 60 V. The transferred membranes were blocked for 1 h in 5% nonfat milk at room temperature and incubated with different primary antibodies (dilution ratio: 1:500) overnight at 4 °C, following by washing and incubating with horseradish peroxidase-conjugated secondary antibodies (dilution ratio: 1:2000) for 2 h at room temperature. The immunoreactive bands were visualized using detection reagents containing PCA and luminol.

RESULTS AND DISCUSSION

Fabrication and Characterization of $Cu_{1.8}S@mSiO_2$ Nanospheres. The synthetic procedure for $Cu_{1.8}S@mSiO_2$ can be divided into three steps. First, oleic acid-stabilized $Cu_{1.8}S$ nanoparticles were synthesized. Subsequently, the hydrophobic $Cu_{1.8}S$ nanoparticles were transferred into an aqueous phase by utilizing surfactant CTAB. The CTAB-stabilized $Cu_{1.8}S$ nanoparticles were coated with mesoporous silica shells through sol−gel reaction, forming $Cu_{1.8}S@mSiO_2$ core−shell nanocomposites. The removal of surfactant CTAB formed mesoporous silica nanospheres embedded with single $Cu_{1.8}S$ nanoparticle.

The XRD pattern of as-obtained hydrophobic $Cu_{1.8}S$ is shown in Figure S1 (Supporting Information). Several obvious diffraction peaks such as (0, 0, 15), (1, 0, 7), (1, 0, 10), (0, 1, 20), and (1, 1, 15) can be clearly seen, which can be ascribed to pure rhombohedral phase $Cu_{1.8}S$ (JCPDS 47-1748). A representative TEM image (Figure 1a) reveals that the hydrophobic $Cu_{1.8}S$ nanoparticles have well-defined shape and uniform size (about 17 nm), which tend to form superlattice structure by self-assembly fashion on the TEM grid. As presented in Figure S2 (Supporting Information), the size distribution of $Cu_{1.8}S$ nanoparticles is in the range of 15−21 nm and the mean size is 17.58 nm, which is consistent with our results. Then after mesoporous silica coating, core−shell structured $Cu_{1.8}S@mSiO_2$ nanospheres were achieved. As shown in Figure 1b, a single $Cu_{1.8}S$ core was encapsulated homogeneously by the mesoporous silica shell and the disordered mesopores. The composite nanospheres have uniform diameter of about 58 nm, in which the thickness of the mesoporous silica shell is about 20 nm.

We further investigated the photothermal effect of $Cu_{1.8}S@mSiO_2$ nanospheres under 980 nm NIR light irradiation. Figure S3 (Supporting Information) shows the UV−vis−NIR absorption spectrum of an aqueous solution containing $Cu_{1.8}S@mSiO_2$ nanospheres (0.5 mg mL^{-1}). It was found that the nanospheres showed a strong and broad NIR absorption band extending well beyond 1100 cm^{-1}, which suffers from localized surface plasma resonances of the vacancy-doped $Cu_{1.8}S$ core.[39] This suggests the potential of $Cu_{1.8}S@mSiO_2$ nanospheres as a kind of efficient NIR absorbing agent for photothermal conversion.[40] Upon irradiation with a NIR laser (980 nm, 1 W cm^{-2}) of an aqueous solution containing $Cu_{1.8}S@mSiO_2$ nanospheres at various concentrations (0, 0.0625, 0.125, 0.25, and 0.5 mg mL^{-1}), temperature changes were observed (Figure 1c). An obvious effect of concentration-dependent temperature elevation was clearly seen. That is, at a concentration of 0.0625 mg mL^{-1}, the NIR light over a period of 300 s induced a temperature increase of $Cu_{1.8}S@mSiO_2$ nanospheres from 19.3 °C to 40.8 °C. In comparison, the temperature of the aqueous solution without $Cu_{1.8}S@mSiO_2$ nanospheres increased to only 29.5 °C. With an increase in concentration, the magnitude of temperature elevation increased gradually (Figure S4, Supporting Information). The solution temperature can reach as high as 60.2 °C with a concentration of 0.5 mg mL^{-1}. Moreover, we measured the shape of nanoparticles after the irradiation for 5 min three times (5 min break after 5 min irradiation) with a 980 nm laser (1 W cm^{-2}). From the TEM image, it can be found that the shape of the sample has no obvious change (Figure S5, Supporting Information). This indicates that the laser irradiation has no influence on the stability of $Cu_{1.8}S$ nanoparticles. Besides, we investigated the in vivo photothermal image of tumor-bearing Balb/c mice treated with and without the $Cu_{1.8}S@mSiO_2$ nanospheres after a 980 nm laser irradiation for 180 s (Figure 1d). After the injection of $Cu_{1.8}S@mSiO_2$ nanospheres, the surface temperature of the tumor sites irradiated with the NIR laser (1 W cm^{-2}) rose swiftly to about 55 °C. In the control experiment, the local temperature of the tumor increased to about 30 °C. These data demonstrated the ability of $Cu_{1.8}S@mSiO_2$ nanospheres to generate a sufficient photothermal conversion effect under NIR light irradiation.

Cellular Uptake of NCs in MCF-7 and HEK-293 Cells. Precise targeting of drug-loaded nanoparticles to the disease tissue is a challenging task.[41] In recent years, single-stranded oligonucleotides aptamers have emerged as a novel class of molecules which rival antibodies in both therapeutic and diagnostic applications.[42] Especially, AS1411, a 26-base DNA oligonucleotide, shows high binding affinity and specificity for the cancer cell membrane-bound overexpressed protein nucleolin and has been used for acute myeloid leukemia and renal carcinoma in phase II clinical trials[43] In this design, $Cu_{1.8}S@mSiO_2$ NCs, which were functionalized with APTES through a hydrolysis reaction on the surface (Figure S6, Supporting Information), were conjugated to a 3′-thiol-

DOI: 10.1021/acsami.5b05522
ACS Appl. Mater. Interfaces 2015, 7, 20696−20706

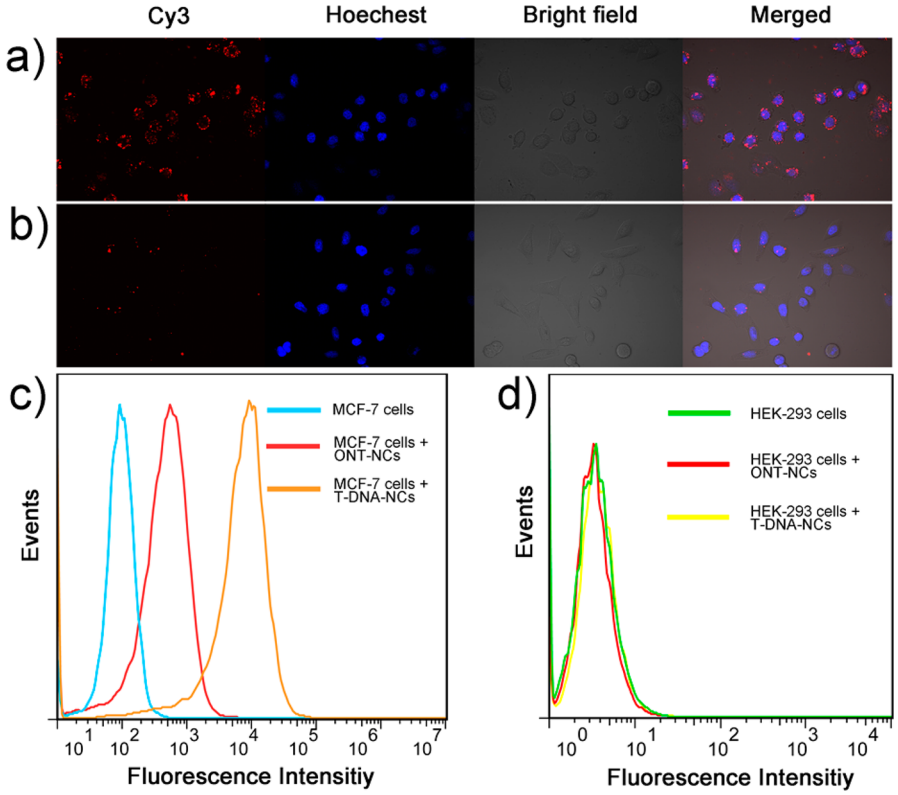

Figure 2. Confocal microscopy images of (a) MCF-7 (targeted cells) cells and (b) HEK-293 cells (control cells) treated with the T-DNA–NCs. Flow cytometry profile of the binding of the T-DNA–NCs and ONT–NCs with (c) MCF-7 cells and (d) HEK-293 cells, respectively.

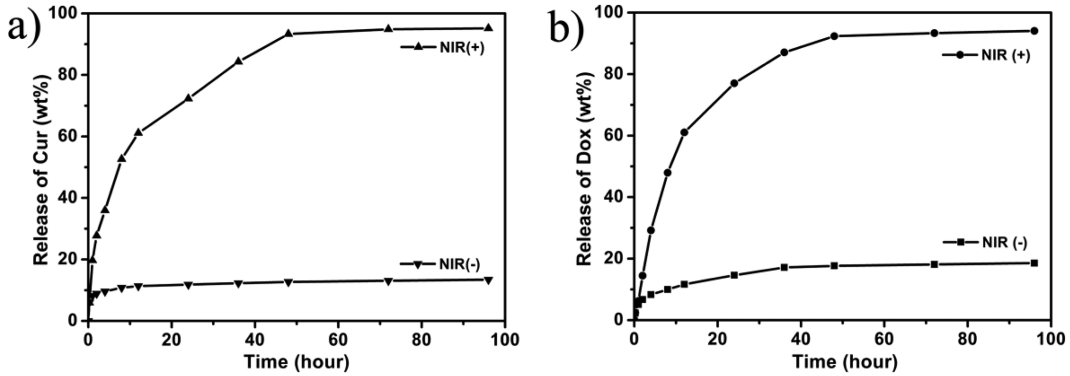

Figure 3. Cumulative (a) Cur and (b) Dox release from T-DNA(Dox)–NC–Cur nanocomposites in pH 7.4 PBS buffer.

functionalized anchor strand with Sulfo-SMCC linker (ONT–NCs), and then AS1411-conjugated targeted strands were linked to anchor strands through a complementary principle of base pairs as targeting ligand and loading sites of Dox (T-DNA–NCs) (Figure S7, Supporting Information).

To examine the capability of T-DNA–NCs to interact with target tumor cells, we visualized the cellular internalization of Cy3-labeled T-DNA–NCs. MCF-7 cells with high nucleolin expression and negative HEK-293 cells without nucleolin were incubated 37 °C for 2 h with targeted (T-DNA–NC–Cy3)/nontargeted (ONT–NC–Cy3) nanocomposites, respectively. The ONT–NC–Cy3/T-DNA–NC–Cy3 nanoparticles showed a significant increase in its binding and uptake fluorescence signal in MCF-7 cells, as evidenced by high-magnification confocal microscopy (Figure 2a), whereas they exhibited much less binding and internalization ability in HEK-293 cells (Figure 2b). These results clearly demonstrated that the T-DNA–NCs had high targeting selectivity for MCF-7 cells. Flow cytometric analysis further validated the targeting specificities of the T-DNA–NC–Cy3 toward MCF-7 cells (Figure 2c). As we have seen, T-DNA–NCs exhibited a higher binding affinity to MCF-7 cells at 37 °C, whereas both ONT–NC and T-DNA–NC showed weak affinity to the negative HEK-293 cells, confirmed by only a small fluorescence peak shift (Figure 2d). These results demonstrated that the aptamer-guided T-DNA–NCs could be effectively endocytosed by the targeting MCF-7 cells but had little affinity to nontargeted cells.

Drug Loading and NIR-Responsive Release of T-DNA–NCs. Dox is a first-line cancer chemotherapeutic agent for various malignancies.[44] However, major adverse effects including liver dysfunction and cardiomyopathy accompanied by multidrug resistance severely limited the use of Dox under clinical conditions.[45] In an effort to overcome the associated

DOI: 10.1021/acsami.5b05522
ACS Appl. Mater. Interfaces 2015, 7, 20696–20706

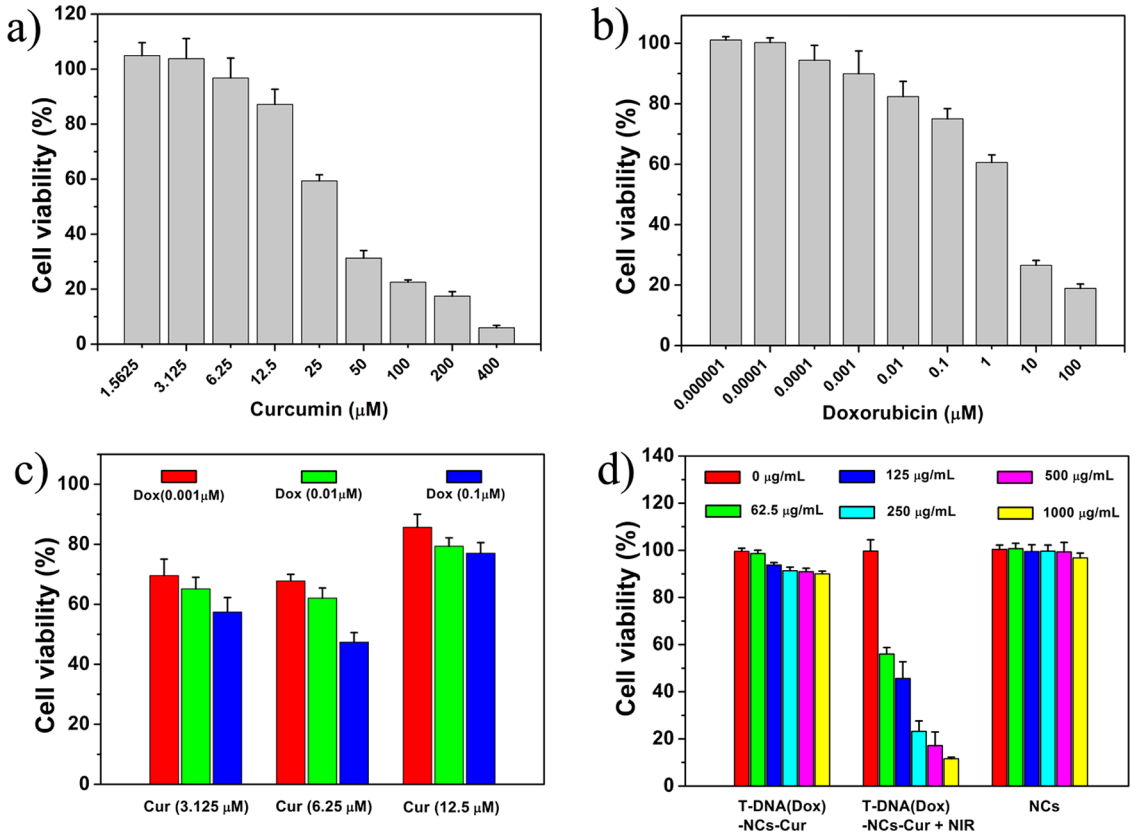

Figure 4. (a) MCF-7 cell viabilities after 24 h of incubation with Cur at different concentrations; (b) MCF-7 cell viabilities after 24 h of incubation with Dox at different concentrations; (c) MCF-7 cell viabilities after 24 h of incubation with Cur−Dox combination at different concentrations; (d) MCF-7 cell viabilities after 24 h of incubation with NCs, T-DNA(Dox)−NC−Cur, or T-DNA(Dox)−NC−Cur and NIR at different concentrations. Error bars indicate standard deviations, $N = 3$.

liver dysfunction and cardiomyopathy, novel coloaded Dox and Cur drug delivery systems were exploited.

To examine the drug delivery, the hydrophobic anticancer drug Cur was encapsulated into the pore of NCs. The resulting NC−Cur is composed of a $Cu_{1.8}S$ core, and the drug-loading rate was calculated to be 23 wt % by measuring the absorption band of Cur at 340 nm. Then the hydrophilic anticancer drug Dox was intercalated into double-strand GC base pairs. The actual drug-loading content of Dox is 6.3 wt % according to the absorption spectrum of Dox at 480 nm. As shown in Figure 3, the Cur and Dox release profiles of Cur- and Dox-loaded T-DNA−NCs in PBS buffer (pH 7.4) under 980 nm NIR irradiation showed similar profiles. Without NIR laser irradiation, only 18% of Dox and 13% Cur were released from the nanocomposite even after 96 h at pH 7.4. Contrarily, upon NIR light irradiation, T-DNA(Dox)−NC−Cur nanocomposites displayed a slow and continuous release of Dox (94%) and Cur (95%) even after 96 h at pH 7.4 due to denaturation of the DNA helix and uncapping of the DNA gatekeeper. In vitro drug release showed that the premature release of Cur from DNA-hybridized T-DNA−NCs was circumvented by the bifunctional helix−aptamer coating as the gatekeeper. As a result, DNA hybridization on the silica-coated nanocomposite surface may offer a new method to solve the premature release and biocompatibility.

In Vitro Cell Toxicity and Synergistic Effects. It has been reported that Cur showed a synergistic effect on Dox in liver cancer cells.[46] The NIR-triggered combined growth-inhibitory effect against tumor cells was investigated by detecting the cell viability using the MTT assay. First, MCF-7 cells were treated with free Cur and Dox or a Cur−Dox combination. We estimated the degree of synergy between free Cur and Dox by characterizing their cytotoxicity toward MCF-7 cells in vitro separately and in combination. The IC_{50} of free Cur or Dox treatment was 46.93 and 1.27 μM, respectively (Figure 4a,b). However, a Cur−Dox combination led to a much lower IC_{50} of 0.25 μM (based on the concentration of Dox) as shown in Figure 4c. The degree of synergy was estimated by a combination index (CI) using the Chou−Talalay isobologram equation.[47] The CI of the free Cur (6.25 μM)−Dox (i.e., 0.001, 0.01, 0.1 μM) combination was 0.32, 0.38, 0.53, respectively, indicating strong synergism. For the Cur- and Dox-loaded NCs, the IC_{50} of T-DNA(Dox)−NC−Cur after exposure to λ = 980 nm laser (2 min, 1 W cm^{-2}) was 0.039 μM (based on the concentration of Dox), which demonstrated 6-fold decreases over the Cur−Dox combination (Figure 4d). However, MCF-7 cells were treated with either core−shell structured NCs, T-DNA(Dox)−NC−Cur (Figure 4d), or NIR irradiation, showing negligible cell death even at concentrations up to 500 μg mL^{-1} after treatment for 24 h. As a result, T-DNA−NCs have good biocompatibility and could be used as drug delivery carriers for biological applications.

ROS Generation of T-DNA(Dox)−NC−Cur upon NIR Irradiation. The accumulation of reactive oxygen species (ROS) inside cells subjected to anticancer drug treatment often represents apoptosis or terminal differentiation.[48] Among the agents upregulating ROS, natural compounds Cur and anticancer chemical drug Dox are crucial inducers of ROS

DOI: 10.1021/acsami.5b05522
ACS Appl. Mater. Interfaces 2015, 7, 20696−20706

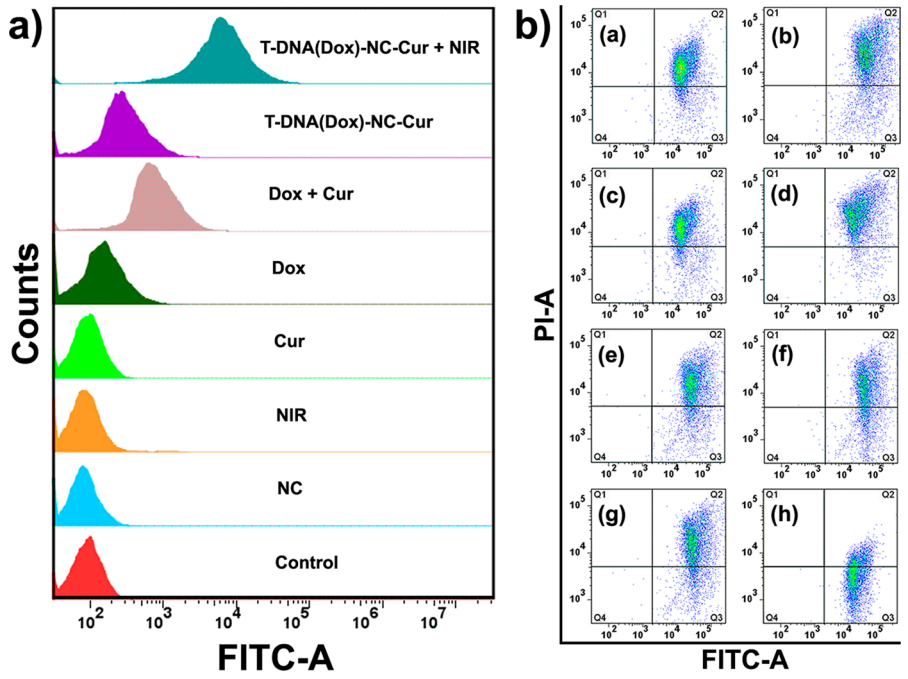

Figure 5. (a) Intracellular ROS generation was determined in MCF-7 cells treated with $Cu_{1.8}S$@$mSiO_2$ NCs, NIR, free Cur, free Dox, Dox−Cur combination, T-DNA(Dox)−NC−Cur, or T-DNA(Dox)−NC−Cur plus 980 nm laser irradiation. The change in intracellular ROS was measured by FACSCalibur flow cytometry. (b) The change in MMP was detected using flow cytometry: (a) control, (b) $Cu_{1.8}S$@$mSiO_2$ NCs alone, (c) NIR, (d) Cur, (e) Dox, (f) Dox−Cur combination, (g) T-DNA(Dox)−NC−Cur, (h) T-DNA(Dox)−NC−Cur plus 980 nm laser irradiation.

correlated with apoptosis.[49] The generation of intracellular ROS was monitored through conversion of nonfluorescent DCFH-DA to fluorescent DCF. After MCF-7 cells were incubated with NCs, NIR, Cur, Dox, Dox−Cur, T-DNA(Dox)−NC−Cur, or T-DNA(Dox)−NC−Cur plus NIR irradiation for 2 h (5 min break after 5 min irradiation, 1 W cm^{-2}), the relative intracellular fluorescence intensity analyzed by FCM allows quantitative comparison of the ROS generation with different treatments. As we have seen, strong fluorescence signals were observed from T-DNA(Dox)−NC−Cur plus NIR irradiation treatment compared to Cur, Dox, or Dox−Cur treatment, but no obvious fluorescence signals were observed from the NCs and NIR treatment. It was inferred that NIR light caused uncapping of the mesopores due to the denaturation of double-strand DNA and triggered the release of anticancer drug from the T-DNA(Dox)−NC−Cur. Thus, T-DNA(Dox)−NC−Cur can serve as promising nanoplatforms for NIR light-triggered drug-synergized therapy.

At present, there is a strong positive correlation between mitochondrial membrane potential (MMP, $\Delta\Psi_m$) and ROS production. Therefore, the change in $\Delta\Psi_m$ was investigated by flow cytometry with a JC-1 probe in MCF-7 cells. As shown in Figure 5b, the MCF-7 cell population treated with NCs, NIR, Dox, Cur, Dox−Cur combination, or T-DNA(Dox)−NC−Cur indicated that a weak downward shift maintained a high MMP. However, after treatment with T-DNA(Dox)−NC−Cur plus NIR light, MCF-7 cells significantly shifted downward, showing a decrease in MMP and mitochondrial damage. The change in the cytofluorimetric pattern suggests that NIR light-triggered synergistic therapy can induce apoptosis through a mitochondria-mediated pathway.

Apoptotic Mechanisms for NIR-Triggered Synergistic Therapy. On the basis of the changes in ROS and $\Delta\Psi_m$ by T-DNA(Dox)−NC−Cur plus NIR irradiation treatment, mitochondria-initiated apoptosis was detected by flow cytometry. As shown in Figure 6a, treatment of cells with either NCs, NIR, Dox (0.001 μM), Cur (6.25 μM), or T-DNA(Dox)−NC−Cur alone did not show early apoptotic cells compared to the control group. Even though Dox−Cur combination reduced 27.3% apoptotic cells in MCF-7 cells, T-DNA(Dox)−NC−Cur plus NIR irradiation treatment resulted in a significant increase in apoptosis accounting for 71.1%. All the results indicated that the NIR-responsive T-DNA(Dox)−NC−Cur platform triggered apoptosis in MCF-7 cells.

To elucidate the possible apoptotic molecular mechanisms of T-DNA(Dox)−NC−Cur plus NIR irradiation on MCF-7 cells, the protein expression of the mitochondria-mediated pathway in MCF-7 cells was measured by Western blotting. The apoptotic activation of mitochondria leads to the oligomerization of adapter proteins and procaspases, resulting in autoactivation of initiator caspases.[50] As shown in Figure 6c, the expression of cytochrome c and apaf-1 increased in a dose-dependent manner, indicating cytochrome c release from the mitochondria to the cytoplasm and the aggregation of the adapter-targeting nanoparticles.[51] In addition, proapoptotic protein Bax and Bak, which could promote the formation of the mitochondrial outer membrane permeabilization pore (MOMPP), upregulated the expression level, whereas anti-apoptotic proteins Bcl-2, Bcl-xL, and Mcl-1, which inhibited the formation of MOMPP, decreased the expression level, indicating that T-DNA(Dox)−NC−Cur significantly upregulated the ratio of Bax/Bcl-2, Bak/Bcl-xL, and Bak/Mcl-1. The high expressive level of cytochrome c due to release to the cytoplasm from the mitochondria facilitated the formation of apoptosomes (apaf-1/cytochrome c), which could recruit and activate the inactive pro-caspase 9. Figure 6b,c further confirmed that pro-caspase 9 was cleaved at conserved internal aspartic residues to generate an active form of caspase 9 through apoptosome cleavage.[52] Caspase 9 cleaves pro-caspase 3 and forms the major executioner caspase, caspase 3, in

DOI: 10.1021/acsami.5b05522
ACS Appl. Mater. Interfaces 2015, 7, 20696−20706

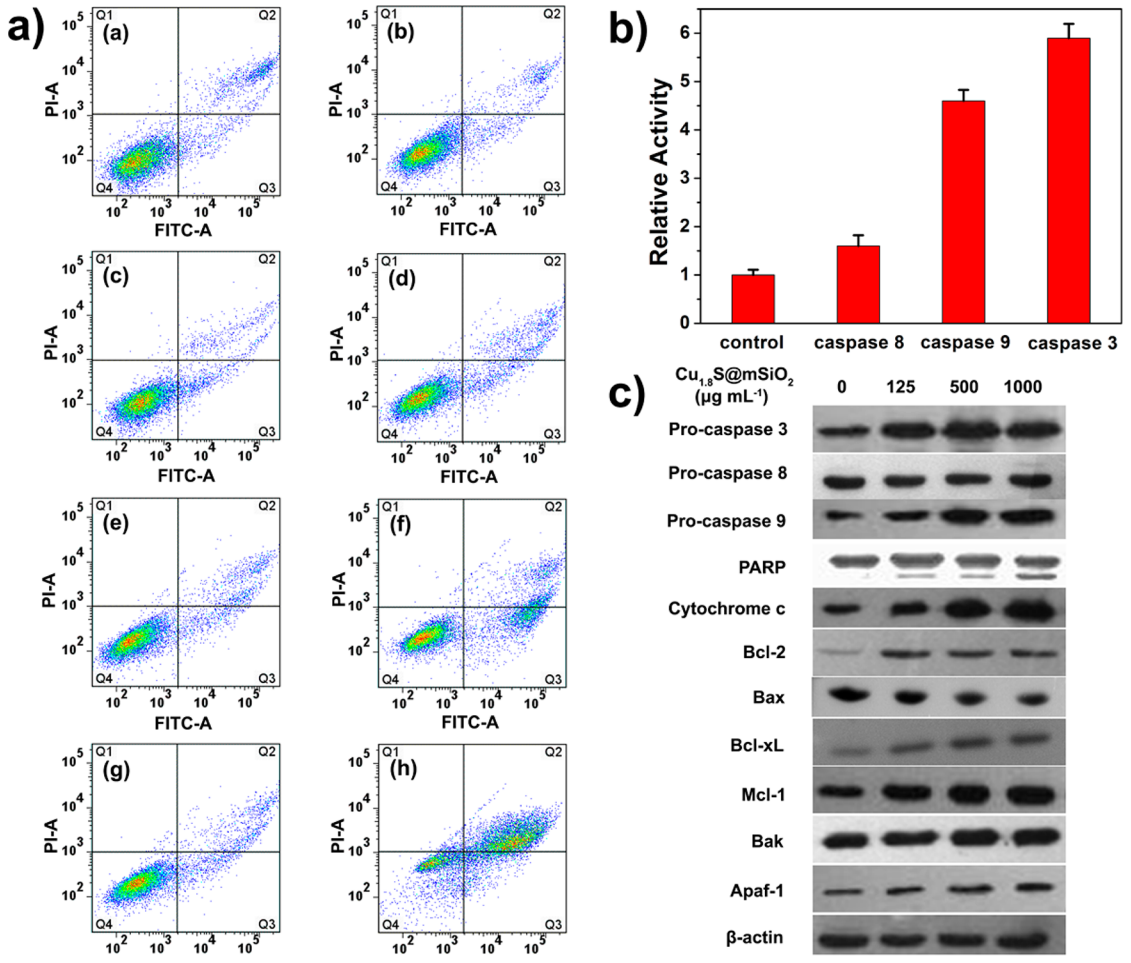

Figure 6. (a) MCF-7 cells were treated with (a) control, (b) $Cu_{1.8}S$@$mSiO_2$ NCs alone, (c) NIR, (d) Cur, (e) Dox, (f) Dox−Cur combination, (g) T-DNA(Dox)−NC−Cur, (h) T-DNA(Dox)−NC−Cur plus 980 nm laser irradiation for 24 h, and annexin V/PI staining was performed. The apoptotic profile is shown. (b) MCF-7 cells were treated with 250 μg/mL T-DNA(Dox)−NC−Cur for 24 h. Relative activity of caspase 3/8/9 was measured. (c) Western blot assay.

different drug-loaded nanocarrier-induced apoptosis nanocarriers.[53,54] The level of pro-caspase 3 decreased significantly after T-DNA(Dox)−NC−Cur plus NIR irradiation treatment, indicating the activation of caspase 3. The activation of the caspase 3 led to a change in the morphological and biochemical features of MCF-7 cells, including DNA fragmentation and cell shrinkage. All the above results suggest that the induction of apoptosis in T-DNA(Dox)−NC−Cur plus NIR irradiation-treated MCF-7 cells may be associated with disruption of mitochondrial function and activation of caspases.

CONCLUSION

In summary, we developed a DNA hybrid, which consists of a $Cu_{1.8}S$ core, a DNA double helix, and an aptamer as a gatekeeper to cap the nanocomposites. The photothermal conversion of copper-based nanoparticles, aptamer-targeted delivery, and NIR-triggered controlled release of the DNA hybrid ascribed to the maximum therapeutic efficacy and minimal side effects. In addition, DNA hybridization on the silica-coated nanocomposite surface improved the biocompatibility of the NCs. A controlled release of Dox and Cur in the combinatory T-DNA−NC delivery system was demonstrated. Therefore, the cytotoxicity of the Cur−Dox combination was considerably enhanced by the T-DNA−NC delivery system. In vitro anticancer results suggest that the codelivery of Dox and Cur reduced the applied dose of the anticancer drugs and the level of procaspase 3 expression and increased the ratio of Bax/Bcl-2, Bak/Bcl-xL, and Bak/Mcl-1, demonstrating a mitochondria-mediated apoptosis (intrinsic pathway) effect and improving the targeting capability of T-DNA−NCs in cancer cells. As a result, this NIR-responsive drug delivery system with combination chemotherapy obtained an optimized therapeutic efficacy in cancer treatment.

ASSOCIATED CONTENT

Supporting Information

The Supporting Information is available free of charge on the ACS Publications website at DOI: 10.1021/acsami.5b05522.

XRD pattern, the size distribution, UV−vis−NIR absorption spectrum, the magnitude of temperature elevation, XPS spectra of different concentrations of $Cu_{1.8}S$@$mSiO_2$, TEM image of $Cu_{1.8}S$ nanoparticles after NIR irradiation, and fluorescence quenching of Dox (PDF)

AUTHOR INFORMATION

Corresponding Authors

*E-mail: jlin@ciac.ac.cn.
*E-mail: cxli@ciac.ac.cn.

DOI: 10.1021/acsami.5b05522
ACS Appl. Mater. Interfaces 2015, 7, 20696−20706

Author Contributions

The manuscript was written through contributions of all authors. All authors have given approval to the final version of the manuscript. Y.Z. and Z.H. contributed equally to this work.

Notes

The authors declare no competing financial interest.

■ ACKNOWLEDGMENTS

This project is financially supported by the National Natural Science Foundation of China (NSFC 51332008, 51372243, 51422209, 51472231, 51472233) and National Basic Research Program of China (2014CB643803).

■ REFERENCES

(1) Avgoustakis, K.; Beletsi, A.; Panagi, Z.; Klepetsanis, P.; Karydas, A.; Ithakissios, G. D. S. PLGA-mPEG Nanoparticles of Cisplatin: *In Vitro* Nanoparticle Degradation, *in Vitro* Drug Release and *in Vivo* Drug Residence in Blood Properties. *J. Controlled Release* **2002**, *79*, 123−135.

(2) Heldin, C.-H.; Rubin, K.; Pietras, K.; Östman, A. High Interstitial Fluid Pressure—An Obstacle in Cancer Therapy. *Nat. Rev. Cancer* **2004**, *4*, 806−813.

(3) Chari, R. V.; Miller, M. L.; Widdison, W. C. Antibody−Drug Conjugates: An Emerging Concept in Cancer Therapy. *Angew. Chem., Int. Ed.* **2014**, *53*, 3796−3827.

(4) Beatty, G. L.; Chiorean, E. G.; Fishman, M. P.; Saboury, B.; Teitelbaum, U. R.; Sun, W.; Huhn, R. D.; Song, W.; Li, D.; Sharp, L. L.; Torigian, D. A.; O'Dwyer, P. J.; Vonderheide, R. H. Cd40 Agonists Alter Tumor Stroma and Show Efficacy against Pancreatic Carcinoma in Mice and Humans. *Science* **2011**, *331*, 1612−1616.

(5) Smalley, K. S.; Haass, N. K.; Brafford, P. A.; Lioni, M.; Flaherty, K. T.; Herlyn, M. Multiple Signaling Pathways Must Be Targeted to Overcome Drug Resistance in Cell Lines Derived from Melanoma Metastases. *Mol. Cancer Ther.* **2006**, *5*, 1136−1144.

(6) Jia, J.; Zhu, F.; Ma, X.; Cao, Z.; Li, Y.; Chen, Y. Z. Mechanisms of Drug Combinations: Interaction and Network Perspectives. *Nat. Rev. Drug Discovery* **2009**, *8*, 111−128.

(7) Lasithiotakis, K. G.; Sinnberg, T. W.; Schittek, B.; Flaherty, K. T.; Kulms, D.; Maczey, E.; Garbe, C.; Meier, F. E. Combined Inhibition of MAPK and mTOR Signaling Inhibits Growth, Induces Cell Death, and Abrogates Invasive Growth of Melanoma Cells. *J. Invest. Dermatol.* **2008**, *128*, 2013−2023.

(8) He, Q. J.; Shi, J. L. MSN Anti-cancer Nanomedicines: Chemotherapy Enhancement, Overcoming of Drug Resistance, and Metastasis Inhibition. *Adv. Mater.* **2014**, *26*, 391−411.

(9) Fan, X.; Zhang, C.; Liu, D. B.; Yan, J.; Liang, H. P. The Clinical Applications of Curcumin: Current State and the Future. *Curr. Pharm. Des.* **2013**, *19*, 2011−2031.

(10) Reuter, S.; Charlet, J.; Juncker, T.; Teiten, M. H.; Dicato, M.; Diederich, M. Effect of Curcumin on Nuclear Factor κB Signaling Pathways in Human Chronic Myelogenous K562 Leukemia Cells. *Ann. N. Y. Acad. Sci.* **2009**, *1171*, 436−447.

(11) Anuchapreeda, S.; Leechanachai, P.; Smith, M. M.; Ambudkar, S. V.; Limtrakul, P. N. Modulation of P-Glycoprotein Expression and Function by Curcumin in Multidrug-Resistant Human KB Cells. *Biochem. Pharmacol.* **2002**, *64*, 573−582.

(12) Romiti, N.; Tongiani, R.; Cervelli, F.; Chieli, E. Effects of Curcumin on P-Glycoprotein in Primary Cultures of Rat Hepatocytes. *Life Sci.* **1998**, *62*, 2349−2358.

(13) Sung, B.; Kunnumakkara, A. B.; Sethi, G.; Anand, P.; Guha, S.; Aggarwal, B. B. Curcumin Circumvents Chemoresistance *in vitro* and Potentiates the Effect of Thalidomide and Bortezomib against Human Multiple Myeloma in Nude Mice Model. *Mol. Cancer Ther.* **2009**, *8*, 959−970.

(14) Yu, L. L.; Wu, J. G.; Dai, N.; Yu, H. G.; Si, J. M. Curcumin Reverses Chemoresistance of Human Gastric Cancer Cells by Downregulating the NF-κB Transcription Factor. *Oncol. Rep.* **2011**, *26*, 1197−1203.

(15) Duan, J.; Mansour, H. M.; Zhang, Y.; Deng, X.; Chen, Y.; Wang, J.; Pan, Y.; Zhao, J. Reversion of Multidrug Resistance by Co-encapsulation of Doxorubicin and Curcumin in Chitosan/Poly(Butyl Cyanoacrylate) Nanoparticles. *Int. J. Pharm.* **2012**, *426*, 193−201.

(16) Safavy, A.; Raisch, K. P.; Mantena, S.; Sanford, L. L.; Sham, S. W.; Krishna, N. R.; Bonner, J. A. Design and Development of Water-Soluble Curcumin Conjugates as Potential Anticancer Agents. *J. Med. Chem.* **2007**, *50*, 6284−6288.

(17) Anand, P.; Kunnumakkara, A. B.; Newman, R. A.; Aggarwal, B. B. Bioavailability of Curcumin: Problems and Promises. *Mol. Pharm.* **2007**, *4*, 807−818.

(18) Yang, P. P.; Gai, S. L.; Lin, J. Functionalized Mesoporous Silica Materials for Controlled Drug Delivery. *Chem. Soc. Rev.* **2012**, *41*, 3679−3698.

(19) Vivero-Escoto, J. L.; Slowing, I. I.; Wu, C. W.; Lin, V. S. Y. Photoinduced Intracellular Controlled Release Drug Delivery in Human Cells by Gold-Capped Mesoporous Silica Nanosphere. *J. Am. Chem. Soc.* **2009**, *131*, 3462−3463.

(20) Zhang, J.; Yuan, Z. F.; Wang, Y.; Chen, W. H.; Luo, G. F.; Cheng, S. X.; Zhuo, R. X.; Zhang, X. Z. Multifunctional Envelope-Type Mesoporous Silica Nanoparticles for Tumor-Triggered Targeting Drug Delivery. *J. Am. Chem. Soc.* **2013**, *135*, 5068−5073.

(21) Xia, T. A.; Kovochich, M.; Liong, M.; Meng, H.; Kabehie, S.; George, S.; Zink, J. I.; Nel, A. E. Polyethyleneimine Coating Enhances the Cellular Uptake of Mesoporous Silica Anoparticles and Allows Safe Delivery of Sirna and DNA Constructs. *ACS Nano* **2009**, *3*, 3273−3286.

(22) Chen, C.; Geng, J.; Pu, F.; Yang, X. J.; Ren, J. S.; Qu, X. G. Polyvalent Nucleic Acid/Mesoporous Silica Nanoparticle Conjugates: Dual Stimuli-Responsive Vehicles for Intracellular Drug Delivery. *Angew. Chem., Int. Ed.* **2011**, *50*, 882−886.

(23) Wu, S. S.; Huang, X.; Du, X. Z. Glucose- and pH-Responsive Controlled Release of Cargo from Protein-Gated Carbohydrate-Functionalized Mesoporous Silica Nanocontainers. *Angew. Chem., Int. Ed.* **2013**, *52*, 5580−5584.

(24) Chaires, J. B.; Herrera, J. E.; Waring, M. J. Preferential Binding of Daunomycin to 5′ATCG and 5′ATGC Sequences Revealed by Footprinting Titration Experiments. *Biochemistry* **1990**, *29*, 6145−6153.

(25) Xiao, Z. Y.; Ji, C. W.; Shi, J. J.; Pridgen, E. M.; Frieder, J.; Wu, J.; Farokhzad, O. C. DNA Self-Assembly of Targeted Near-Infrared-Responsive Gold Nanoparticles for Cancer Thermo-Chemotherapy. *Angew. Chem., Int. Ed.* **2012**, *51*, 11853−11857.

(26) Fang, Y.; Zheng, G. F.; Yang, J. P.; Tang, H. S.; Zhang, Y. F.; Kong, B.; Lv, Y. Y.; Xu, C. J.; Asiri, A. M.; Zi, J.; Zhang, F.; Zhao, D. Y. Dual-Pore Mesoporous Carbon@Silica Composite Core-Shell Nanospheres for Multidrug Delivery. *Angew. Chem.* **2014**, *126*, 5470−5474.

(27) Zhang, P. H.; Cheng, F. F.; Zhou, R.; Cao, J. T.; Li, J. J.; Burda, C.; Min, Q. H.; Zhu, J. J. DNA-Hybrid-Gated Multifunctional Mesoporous Silica Nanocarriers for Dual-Targeted and MicroRNA-Responsive Controlled Drug Delivery. *Angew. Chem.* **2014**, *126*, 2403−2407.

(28) Wang, L.; Dong, H.; Li, Y.; Xue, C.; Sun, L.-D.; Yan, C.-H.; Li, Q. Reversible Near-Infrared Light Directed Reflection in a Self-Organized Helical Superstructure Loaded with Upconversion Nanoparticles. *J. Am. Chem. Soc.* **2014**, *136*, 4480−4483.

(29) Ehlert, O.; Thomann, R.; Darbandi, M.; Nann, T. A. Four-Color Colloidal Multiplexing Nanoparticle System. *ACS Nano* **2008**, *2*, 120−124.

(30) Ostrowski, A. D.; Chan, E. M.; Gargas, D. J.; Katz, E. M.; Han, G.; Schuck, P. J.; Milliron, D. J.; Cohen, B. E. Controlled Synthesis and Single-Particle Imaging of Bright, Sub-10 nm Lanthanide-Doped Upconverting Nanocrystals. *ACS Nano* **2012**, *6*, 2686−2692.

(31) Yang, J. P.; Shen, D.; Zhou, L.; Li, W.; Li, X. M.; Yao, C.; Wang, R.; El-Toni, A. M.; Zhang, F.; Zhao, D. Y. Spatially Confined Fabrication of Core-Shell Gold Nanocages@Mesoporous Silica for

DOI: 10.1021/acsami.5b05522
ACS Appl. Mater. Interfaces 2015, 7, 20696−20706

Near-Infrared Controlled Photothermal Drug Release. *Chem. Mater.* **2013**, *25*, 3030−3037.
(32) Yuan, Q.; Wu, Y.; Wang, J.; Lu, D. Q.; Zhao, Z. L.; Liu, T.; Zhang, X. B.; Tan, W. H. Targeted Bioimaging and Photodynamic Therapy Nanoplatform Using an Aptamer-Guided G-Quadruplex DNA Carrier and Near-Infrared Light. *Angew. Chem., Int. Ed.* **2013**, *52*, 13965−13969.
(33) Tian, Q. W.; Hu, J. Q.; Zhu, Y. H.; Zou, R. J.; Chen, Z. G.; Yang, S. P.; Li, R. W.; Su, Q. Q.; Han, Y.; Liu, X. G. Sub-10 nm Fe_3O_4@$Cu_{2-x}S$ Core−Shell Nanoparticles for Dual-Modal Imaging and Photothermal Therapy. *J. Am. Chem. Soc.* **2013**, *135*, 8571−8577.
(34) Young, J. K.; Figueroa, E. R.; Drezek, R. A. Tunable Nanostructures as Photothermal Theranostic Agents. *Ann. Biomed. Eng.* **2012**, *40*, 438−459.
(35) Michalet, X.; Pinaud, F. F.; Bentolila, L. A.; Tsay, J. M.; Doose, S.; Li, J. J.; Sundaresan, G.; Wu, A. M.; Gambhir, S. S.; Weiss, S. Quantum Dots for Live Cells, *in Vivo* Imaging, and Diagnostics. *Science* **2005**, *307*, 538−544.
(36) Zhou, J. H.; Rossi, J. J. Cell-type-specific, Aptamer-functionalized Agents for Targeted Disease Therapy. *Mol. Ther.–Nucleic Acids* **2014**, *3*, e169.
(37) Liu, L. G.; Zhong, H. Z.; Bai, Z. L.; Zhang, T.; Fu, W. P.; Shi, L. J.; Xie, H. Y.; Deng, L. G.; Zou, B. S. Controllable Transformation from Rhombohedral $Cu_{1.8}S$ Nanocrystals to Hexagonal CuS Clusters: Phase- and Composition-Dependent Plasmonic Properties. *Chem. Mater.* **2013**, *25*, 4828−4834.
(38) Chen, Y. Y.; Hou, Z. Y.; Liu, B.; Huang, S. S.; Li, C. X.; Lin, J. DOX-Cu_9S_5@mSiO_2-PG Composite Fibers for Orthotopic Synergistic Chemo- and Photothermal Tumor Therapy. *Dalton Trans.* **2015**, *44*, 3118−3127.
(39) Luther, J. M.; Jain, P. K.; Ewers, T.; Alivisatos, A. P. Localized Surface Plasmon Resonances Arising from Free Carriers in Doped Quantum Dots. *Nat. Mater.* **2011**, *10*, 361−366.
(40) Song, G.; Wang, Q.; Wang, Y.; Lv, G.; Li, C.; Zou, R.; Chen, Z.; Qin, Z.; Huo, K.; Hu, R. G.; Hu, J. Q. A Low-Toxic Multifunctional Nanoplatform Based on Cu_9S_5@mSiO_2 Core-Shell Nanocomposites: Combining Photothermal- and Chemotherapies with Infrared Thermal Imaging for Cancer Treatment. *Adv. Funct. Mater.* **2013**, *23*, 4281−4292.
(41) Bisker, G.; Yeheskely-Hayon, D.; Minai, L.; Yelin, D. Controlled Release of Rituximab from Gold Nanoparticles for Phototherapy of Malignant Cells. *J. Controlled Release* **2012**, *162*, 303−309.
(42) Du, Y.; Li, B. L.; Wang, E. K. "Fitting" Makes "Sensing" Simple: Label-Free Detection Strategies Based on Nucleic Acid Aptamers. *Acc. Chem. Res.* **2013**, *46*, 203−213.
(43) Bates, P. J.; Laber, D. A.; Miller, D. M.; Thomas, S. D.; Trent, J. O. Discovery and Development of the G-rich Oligonucleotide AS1411 as a Novel Treatment for Cancer. *Exp. Mol. Pathol.* **2009**, *86*, 151−164.
(44) Jordon, M. A. Mechanism of Action of Antitumor Drugs that Interact with Microtubules and Tubulin. *Curr. Med. Chem.: Anti-Cancer Agents* **2002**, *2*, 1−17.
(45) Chatterjee, K.; Zhang, J. Q.; Honbo, N.; Karliner, J. S. Doxorubicin Cardiomyopathy. *Cardiology* **2010**, *115*, 155−162.
(46) Liu, W.; Chen, Q.; Zhao, X.; Li, Y.; Tang, H.; Liu, X.; Yang, X. Codelivery of Doxorubicin and Curcumin with Lipid Nanoparticles Results in Improved Efficacy of Chemotherapy in Liver Cancer. *Int. J. Nanomed.* **2014**, *10*, 257−270.
(47) Chou, T. C.; Motzer, R. J.; Tong, Y.; Bosl, G. J. Computerized Quantitation of Synergism and Antagonism of Taxol, Topotecan, and Cisplatin against Human Teratocarcinoma Cell Growth: A Rational Approach to Clinical Protocol Design. *J. Natl. Cancer. Inst.* **1994**, *86*, 1517−1524.
(48) Watson, A. S.; Mortensen, M.; Simon, A. K. Autophagy in the Pathogenesis of Myelodysplastic Syndrome and Acute Myeloid Leukemia. *Cell Cycle* **2011**, *10*, 1719−1725.
(49) Kang, J.; Chen, J.; Shi, Y.; Jia, J.; Zhang, Y. Curcumin-Induced Histone Hypoacetylation: The Role of Reactive Oxygen Species. *Biochem. Pharmacol.* **2005**, *69*, 1205−1213.
(50) Green, D. R.; Reed, J. C. Mitochondria and Apoptosis. *Science* **1998**, *281*, 1309−1312.
(51) Antonsson, B.; Conti, F.; Ciavatta, A.; Montessuit, S.; Lewis, S.; Martinou, I.; Bernasconi, L.; Bernard, A.; Mermod, J. J.; Mazzei, G.; Maundrell, K.; Gambale, F.; Sadoul, R.; Martinou, J. C. Inhibition of Bax Channel-forming Activity by Bcl-2. *Science* **1997**, *277*, 370−372.
(52) Dejean, L. M.; Martinez-Caballero, S.; Kinnally, K. W. Is MAC the Knife that Cuts Cytochrome *c* from Mitochondria During Apoptosis? *Cell Death Differ.* **2006**, *13*, 1387−1395.
(53) Liu, Y.; Hu, Y. Z.; Guo, Y. B.; Ma, H. J.; Li, J. F.; Jiang, C. Targeted Imaging of Activated Caspase-3 in the Central Nervous System by a Dual Functional Nano-Device. *J. Controlled Release* **2012**, *163*, 203−210.
(54) Agrawal, S. S.; Saraswati, S.; Mathur, R.; Pandey, M. Cytotoxic and Antitumor Effects of Brucine on Ehrlich Ascites Tumor and Human Cancer Cell Line. *Life Sci.* **2011**, *89*, 147−158.

DOI: 10.1021/acsami.5b05522
ACS Appl. Mater. Interfaces 2015, 7, 20696−20706